NJC

C2 weakens turn over frequency during melting of FexCy: insights from reactive MD simulations

Journal:	*New Journal of Chemistry*
Manuscript ID	NJ-ART-10-2021-005114
Article Type:	Paper
Date Submitted by the Author:	27-Oct-2021
Complete List of Authors:	Liu, Yubing; Beijing University of Chemical Technology, Lu, Kuan; Chinese Academy of Sciences State Key Laboratory of Coal Conversion Liu, Xingchen; Institute of Coal Chemistry Chinese Academy of Sciences, Liu, Jinjia; Institute of Coal Chemistry Chinese Academy of Sciences, State Key Laboratory of Coal Conversion Guo, Wenping; National Energy Center for Coal to Clean Fuels, Synfuels China Co., Ltd, Huairou District, Beijing, 101400, P.R. China; Chen, Wei; Beijing University of Chemical Technology, State Key Laboratory of Chemical Resource Engineering Peng, Qing; University of Michigan, ; Wuhan University, Song, Yu-Fei; State Key Laboratories of Chemical Resource Engineering, Chemistry Yang, Yong; Synfuels CHINA, National Energy Center for Coal to Liquids; Institute of Coal Chemistry CAS, State Key Laboratory of Coal Conversion Li, Yongwang; Institute of Coal Chemistry, Synfuels China Wen, Xiaodong; Institute of Coal Chemistry Chinese Academy of Sciences, Coal Conversion; Synfuels China Technology Co Ltd, Research and Development

C2 weakens turn over frequency during melting of Fe_xC_y: insights from reactive MD simulations

Yubing Liu,[a,b,c] Kuan Lu,*[b,c] Xingchen Liu,[b,c] Jinjia Liu,[b,c,d] Wen-Ping Guo,[c] Wei Chen,[a] Qing Peng,[e] Yu-Fei Song,*[a] Yong Yang,[b,c] Yong-Wang Li,[b,c] and Xiao-Dong Wen*[b,c]

[a]State Key Laboratory of Chemical Resource Engineering, School of Chemistry, Beijing University of Chemical Technology, Beijing 100029, P. R. China

[b]State Key Laboratory of Coal Conversion, Institute of Coal Chemistry, Chinese Academy of Sciences, Taiyuan, Shanxi 030001, P.R. China

[c]National Energy Center for Coal to Clean Fuels, Synfuels China Co., Ltd., Huairou District, Beijing 101400, P. R. China

[d]University of Chinese Academy of Sciences, No. 19A Yuquan Road, Beijing 100049, P. R. China

[e]Physics Department, King Fahd University of Petroleum & Minerals, Dhahran 31261, Saudi Arabia

Abstract: The first-order phase transition plays a pivotal role in material behaviors, yet that of carbides, a type of important materials, has not been systematically studied. Herein, the melting process and structural properties of binary iron carbide (Fe_xC_y) nanoparticles are characterized by reactive molecular dynamics simulation. It was found that the melting point of Fe_xC_y nanoparticle decreased with decreasing size and increased with increasing Fe/C ratio, which were consistent with the experimental results. The melting process starts at the surface and proceeds inwards. The carbon atoms are fully activated before reaching the melting point and the iron core melts last. At high temperatures, carbon atoms exhibit significant outward diffusion behavior and form carbon deposition on the surface. When the temperature exceeds the pre-melting point, although the high temperature gives the nanoparticles more atomic active sites with low coordination, the surface carbon accumulation, such as C2, blocks the active sites leading to a lower turn-over frequency of Fe_xC_y for CO dissociation. These findings provide an atomistic comprehension of the melting mechanisms and behaviors of binary Fe_xC_y nanoparticles, as well as a theoretical foundation for understanding their structural transformation as a catalyst, which is caused by the heat released from catalytic exothermic reactions.

Keywords: RMD, Fe_xC_y nanoparticles, Melting behavior, Structural evolution, TOF

1. Introduction

Melting is a first-order phase transition and pivotal material behavior happening in daily life. Compared with bulk materials, nanomaterials posses unique properties and more complex melting behaviors due to the large surface/volume ratio of their nanoparticles.[1-5] For example, the melting point of nanomaterials depends on particle size.[6-8] Nanometer clusters and nanoparticles have been extensively studied in recent years.[9-12] Precisely probing and predicting their variations during melting has become possible due to the rapid development of experimental and computational techniques.[13-16] Iron is an essential metal in the industry due to its excellent properties, low cost, and wide availability. Nano iron is widely used as a highly active catalyst in industrial-scale catalysis for Fischer-Tropsch synthesis (FTS),[17,18] bioimaging,[19] and energetic materials.[20] Melting point is one of the most basic properties of nano iron and the systematic investigation of its melting behaviors can better understand its catalytic and mechanical properties.

The thermodynamic properties of nanoparticles, such as melting and atomic diffusion, are critical to their synthesis, characterization, and application. However, it is difficult to measure their melting points experimentally. However, the rapid development of molecular dynamics simulation methods in the past decade has allowed researchers to conduct large-scale studies on the melting process of nano iron. Sun et al.[21] investigated the effects of size of Fe nanoparticles on melting temperature by the ReaxFF force field and found that the defects provide additional energy storage to the Fe nanoparticles for the first time. Shu et al.[22] characterized the melting process of Fe nanoparticles by replica-exchange molecular dynamics (REMD) and demonstrated that REMD could effectively overcome the superheating and undercooling problems. They accurately predicted the melting temperature of Fe nanoparticles and described the size dependence of the melting temperature with a revised liquid skin melting (LSM) model. Ding et al.[23] studied the surface melting behaviors of Fe clusters by constant temperature molecular dynamics simulation based on many-body interaction potential. The study revealed that the melting surface layer gradually became thicker during

heating and the cluster lattice suddenly collapsed and a phase transition occurred at the critical temperature. Joshi et al.[24] found by an embedded atom method (EAM) potential that the melting points of Fe and Ni nanoparticles were particle size-dependent, and the critical temperatures were linearly related to the inverse of particle size.

In addition to the discoveries mentioned above, these studies also suggest that the melting initially happens on the surface of nanoparticle and then extends to the whole nanoparticle. The surface pre-melting at the initial stage changes the nanoparticle surface structure and significantly affects its properties, especially the catalytic performance, which has been reported by extensive studies on the evolution of surface morphologies of various catalysts during reactions.[25-29] In particular, many typical industrial catalytic reactions, such as the activation of methane and the oxidation of ammonia over transition metal nano catalysts, occur at high temperatures (over 1000 K),[30-32] which may has reconstructed the surface of catalyst by pre-melting process in the reaction conditions. Therefore, understanding the dynamic evolution of the surface structure of nano-catalyst particles under real reaction conditions is essential for catalyst design. In the previous work, we systematically studied the surface pre-melting activities of 11 transition metal nanoparticles by molecular dynamics simulation using EAM potential.[33] Our study revealed that the surface pre-melting of 3 nm Fe nanoparticles occurred at 1050 K. The activated atoms can further activate other atoms using the excess kinetic energy, and the resulting activated surface provide more active sites with different atomic coordination numbers, which illustrates the potential impacts of surface pre-melting on heterogeneous catalysis.

Currently, the Fe-based compounds instead of pure iron are more widely used in industry.[19,34-37] The increased interaction and coupling between atoms may complicate the thermodynamic processes, such as melting and atomic diffusion. For instance, the Fe-based catalyst for FTS reaction is generally exposed to the syngas containing CO, H_2, etc.,[17,18,38-40] which results in complex carbide phases under different reaction conditions, especially accompanied by the release of a large amount of heat during the reaction.[41] The heat dissipation of nanoparticle is relatively slow under the cover of gas,

and the resultant local high temperature can change the surface morphology of the nanoparticle and further affect the catalytic performance.[42] An important example is that high temperature can significantly affect the existence of carbon atoms on the catalyst surface, such as carbon-rich surface, carbon-free surface, carbon vacancy, etc., which in turn affect processes such as methanation, hydrogenation, water gas shift, and FTS.[17,43] Niemantsverdriet et al.[44] found that in the carbon-rich (001) surface of Fe_5C_2, CO is difficult to dissociate, while the hydrogenation of surface carbon to CH is a relatively easy reaction process. Carbon-free surface facilitates the direct dissociation of CO. On surfaces containing some carbon vacancies, hydrogen-assisted CO dissociation is more favorable than direct dissociation of CO. In addition, carbon-containing species undergo decomposition and polymerization to generate carbon deposition on the catalyst surface. It could clog the surface active site and lead to deactivation of the catalyst.[45,46] Also, carbon atoms can strength the mechanic properties of Fe-based materials, but inevitably causes chemical inertness.[47,48] Therefore, iron carbide (Fe_xC_y) is also usually used as a constituent in metal alloys and cemented carbide coatings.[49-52] Understanding the melting behavior of Fe_xC_y nanoparticle is important for revealing the interaction between Fe and C in the practical industrial productions.

Due to the complex phase composition of Fe_xC_y catalyst, it is very difficult to characterize and confirm the real active phase with experimental methods.[41] Moreover, the phase changes with the environment, which leads to misinterpretation and misunderstanding of the experimental results.[53] Therefore, the present work was aimed to provide an atomistic understanding of the structural evolution of the Fe_xC_y nanoparticle catalyst during its melting process by the reactive molecular dynamics (RMD) simulation. The models of Fe_xC_y nanoparticles with the sizes ranging from 2 nm to 8 nm and different Fe/C ratios including ε-Fe_2C, χ-Fe_5C_2, θ-Fe_3C, and Fe_4C were constructed. Its effects of size and carbon content on melting temperature, and corresponding structure changes and atomic behaviors during melting were analyzed.

The CO dissociation, a key step in FTS, was also studied to understand the effect of melting on the catalytic activity of Fe_xC_y nanoparticles.

2. Method

The Lindemann index[54] measures the vibration of atoms by calculating a function of interatomic distance in the first neighbor shell. It is widely used to study the melting behavior.[55-58] In general, a high Lindemann index indicates high vibrational motion which means that active atoms are prone to leave their equilibrium sites. It could be seen as an indicator of the melting point when the Lindemann index abruptly ascends. The index is defined as Eq. (1) and (2):

$$\delta = \frac{1}{N}\sum_i \delta_i \quad (1)$$

$$\delta_i = \frac{1}{N-1}\sum_{j \neq i} \frac{\sqrt{\langle r_{ij}^2 \rangle_T - \langle r_{ij} \rangle_T^2}}{\langle r_{ij} \rangle_T} \quad (2)$$

where δ is the globe Lindemann index, δ_i is the local Lindemann index of atom i, N is the number of atoms, r_{ij} is the interatomic distance between atom i and j, and $\langle\rangle_T$ denotes the thermal average of a series of trajectories at temperature T. It has been shown that δ below 0.1 represents an ordered solid structure and above 0.1 transforms into a liquid state. This is referred to as the Lindemann criterion for melting.[54,59,60] According to the temperature dependence of the Lindemann index in Fig. S1, both Fe and C atoms are activated and diffuse to new positions when their Lindemann indices exceed 0.1. Therefore, the critical values can be determined as 0.1 for melting of Fe and C atoms. Here, the pre-melting point is defined as the temperature at which the Lindemann indices of at least three atoms are larger than 0.1.

Information about the melting properties of the Fe_xC_y nanoparticles can be derived from RMD simulations.[61,62] Iron carbides can be formed by the reduction of Fe_2O_3, with α-Fe as an intermediate phase. They have different crystal structures at different temperatures and carbon chemical potentials (μ_C).[41] In iron carbide, the hexagonal

close-packed structure of Fe is distorted with carbon atoms occupying its vacancies. In χ-Fe_5C_2 and θ-Fe_3C, carbon atoms are interspersed into the trigonal voids composed of iron atoms, while carbon atoms occupy octahedral vacancies of ε-Fe_2C and Fe_4C. (Fig. S2a) The nanoparticles with diameters of 2 nm (~ 300 atoms), 3 nm (~ 1100 atoms), 5 nm (~ 5000 atoms) and 8 nm (~ 20000 atoms) sizes were constructed for each of the four structured Fe_xC_y phases (Fe_2C, Fe_5C_2, Fe_3C, and Fe_4C). The nanoparticles are created through Wulff Construction[63] and some relatively stabled surfaces under adiabatic conditions are selected from Zhao et al.[64,65] (Fig. S2b) All the simulations were implemented by RMD using Large-scale Atomic/Molecular Massively Parallel Simulator (LAMMPS)[66] and the corresponding structure changes were observed by Open Visualization Tool (OVITO).[67] The reactive force field (ReaxFF) parameters are derived from our previous work and have been proven to be suitable for describing the Fe-C-O interactions.[40,68,69] The periodic simulation box size was 12 nm × 12 nm × 12 nm. (Fig. S3a) For melting simulations, all the nanoparticles were initially pre-equilibrated at 300 K for 100 ps with canonical (NVT) ensemble. These well-equilibrated structures were then heated up from 300 K to 2000 K for further investigation. Each system lasted for 300 ps with a 0.25 fs time step. For CO activation simulations, the nanoparticle structures simulated at different temperatures were quickly heating or quenching to 800 K and then equilibrated for 10 ps before CO activation reactions. The periodic simulation box has a size of 10.7 nm × 10.7 nm × 10.7 nm including a Fe_5C_2 nanoparticle and 500 CO. (Fig. S3b) Its initial pressure is about 4.6 MPa. The CO activation simulations were run at 800 K for 200 ps. These conditions inhibit the swift evolution of elected temperature structures but accelerate the collision of CO with the nanoparticles, allowing us to accurately examine the effect of melting on the catalytic performance of Fe_xC_y nanoparticles. The velocity Verlet integrator has been employed.

3. Results

3.1. Melting and Surface Pre-melting

Fig. S4 shows the curves of temperature, total energy and potential energy of bulk Fe_5C_2 with time. From these curves it can be deduced that the melting point is 1910 K. However, the Lindemann index is a more definite melting criterion, and more information can be obtained. To explore the melting mechanism of Fe_xC_y nanoparticles, the Lindemann index is introduced to characterize the surface pre-melting behaviors and the structural evolution during melting. The Lindemann indexes of the nanoparticles with different structures and sizes from 300 K to 2000 K are calculated.

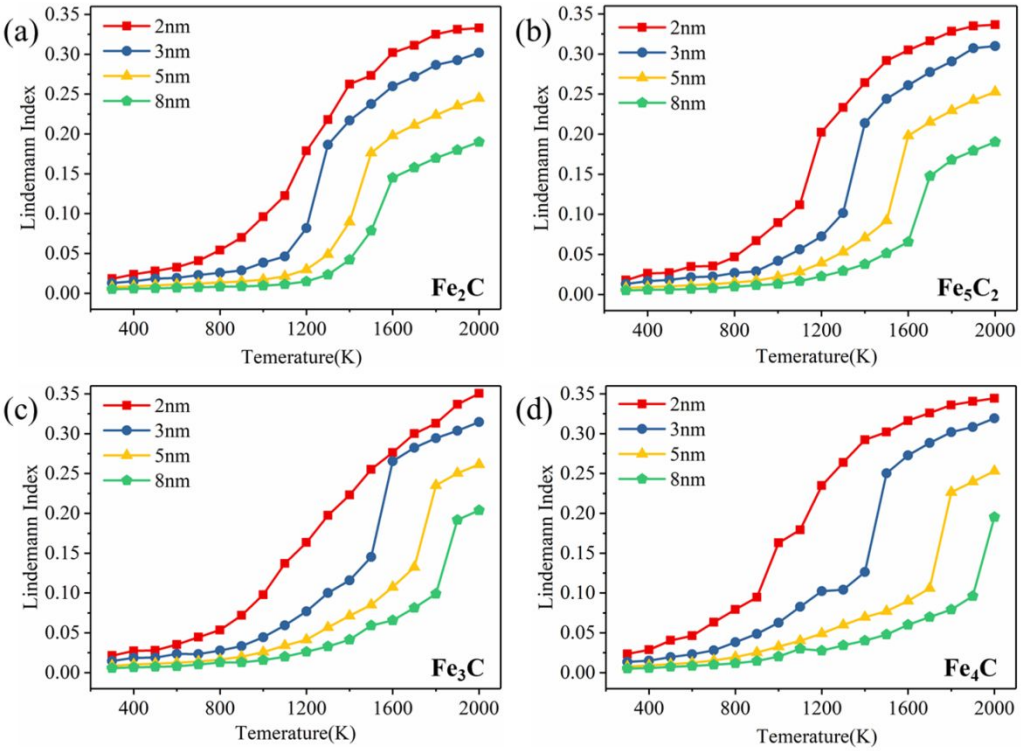

Fig. 1. Overall Lindemann Index of different sizes of Fe_xC_y nanoparticles: (a) Fe_2C; (b) Fe_5C_2; (c) Fe_3C; (d) Fe_4C.

Fig. 1 shows the temperature dependence of the overall Lindemann index of Fe_xC_y nanoparticles from 2 nm to 8 nm. Similar to pure iron clusters, the melting process of most Fe_xC_y nanoparticles can be divided into three stages.[23] In the first stage, the Lindemann index increases linearly and slowly with temperature increasing. The nanoparticle keeps a solid-state, and all atoms vibrate only near their equilibrium positions. In the early of the second stage, the rising trend of the Lindemann index increases (pre-melting process). Some surface atoms can obtain enough kinetic energy

to overcome the binding energy at the initial position and diffuse to other positions on the surface due to its low coordination number when a certain temperature is reached. As the temperature further increases, the kinetic energy of the surface atoms is transferred inward, causing the internal atoms to gradually leave their equilibrium positions and begin to migrate. When the Lindemann index reaches around 0.1, the gradient of the Lindemann line suddenly increases, which indicates the occurrence of the melting process and is also used to judge the melting point of nanoparticles. It is noted that the Lindemann indices of some nanoparticles undergoing melting ranges from 0.1 to 0.15, which is because there are still some internal solid atoms with Lindemann index less than 0.1 when the overall Lindemann index reaches 0.1. After exceeding the threshold of its individual critical temperature, the Lindemann line continuously increases resemble its initial increasing form until the nanoparticle completely melted. At this time, the third stage has also been reached, the Lindemann line is flattening again, and the nanoparticles are in a liquid form totally.

The melting point of nanoparticles exhibits a strong size effect. Compared with large-sized nanoparticles, the Lindemann indices of small-sized particles increase faster with temperature. Due to the larger surface area to volume ratio, they are easier to be fully activated. As the particle size increased, the surface atomic percentage decreases, and higher temperatures are required for the melting of nanoparticles.[70,71] Taking Fe_5C_2 as an example, the critical temperatures of the nanoparticles with the sizes of 2 nm, 3 nm, 5 nm, and 8 nm are 1125 K, 1380 K, 1570 K, and 1700 K, respectively. It can be predicted that the critical temperature will become higher as the particle size further increased. In addition, the melting points obtained by the potential energy are consistent with the results of the Lindemann index. (Figure S5a) The density of nanoparticles decreases gradually with increasing temperature, increases in magnitude above the pre-melting point, and decreases sharply near the melting point. (Figure S5b) This is consistent with the pattern of density change of nanoparticles during melting in the previous works.[72,73] The density of Fe_3C calculated by ReaxFF at low temperature (7.775 g/cm^3) is agreement with the report in the experimental work (~ 7.68 g/cm^3).[74,75]

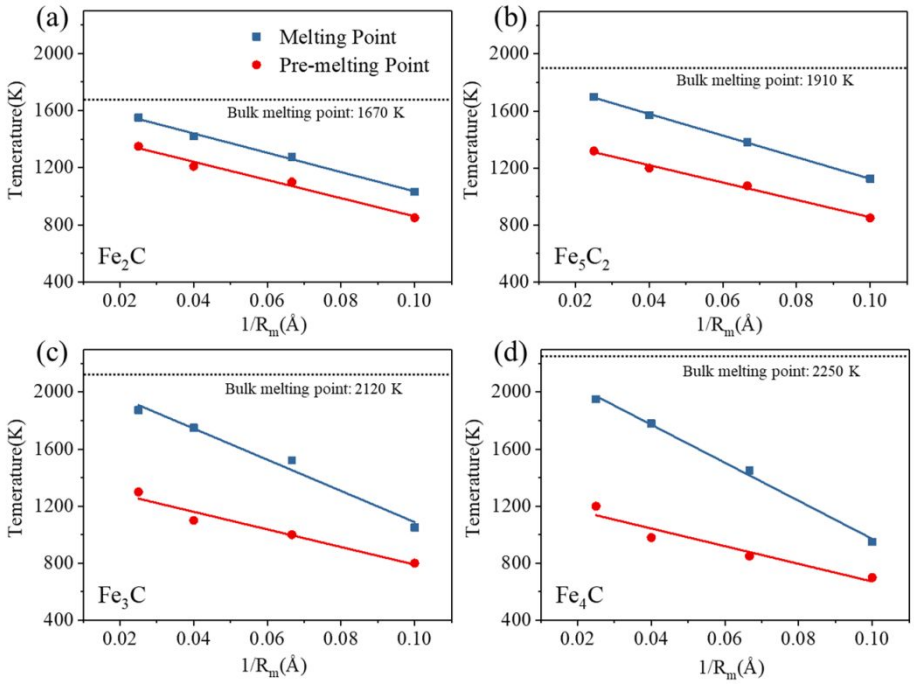

Fig. 2. Melting points and surface melting points of different size of Fe_xC_y nanoparticles: (a) Fe_2C; (b) Fe_5C_2; (c) Fe_3C; (d) Fe_4C. The black dashed line represents the melting temperature of the bulk Fe_xC_y.

Here, we summarize the dependence of the melting and surface pre-melting point of Fe_xC_y nanoparticles on its size. Liu et al.[33] reported that the melting point and pre-melting point of pure metal nanoparticles is linearly related to the inverse of the nanoparticle radius ($1/R_m$). Similar relationship is found in the two-component iron carbide nanoparticles in our work, as shown in Fig. 2. The differences between the melting point and the surface pre-melting point of the Fe_2C nanoparticles with different particle sizes are all ~ 200 K. As the Fe/C ratio increases, that is, the carbon content declines, the difference becomes size dependent. The pre-melting point of the 8 nm Fe_5C_2 nanoparticles is 380 K lower than its melting point and the difference between the pre-melting and melting points of the 2 nm nanoparticles is only ~270 K. As the Fe/C ratio further increased, the size dependence of the difference between pre-melting and melting points becomes more obvious. The differences for 8 nm Fe_3C and Fe_4C nanoparticles reach 575 K and 750 K, respectively. Therefore, it can be concluded that

carbon content plays a very important role in the melting process of Fe_xC_y nanoparticles. The detailed discussion will be present in Section 3.2. The linear relationship may be used to estimate the surface activation temperature of Fe_xC_y nanoparticles based on their melting temperature. In addition, it is found that relatively large (5 nm and 8 nm) nanoparticles with low carbon contents exhibit wider temperature ranges where the solid and liquid phases coexist. The lower the Fe/C ratio (higher the carbon content), the lower the melting point, which is applicable to larger nanoparticles, but not to smaller ones due to their low atomic numbers. (Table S1) The bulk melting temperatures of Fe_2C, Fe_5C_2, Fe_3C and Fe_4C are 1670 K, 1910 K, 2120 K, and 2250 K, respectively. In the experiment, the bulk melting temperature of Fe_3C is 2055 K.[76] Our conclusion is consistent to the work reported by Xi et al.[77] that increasing carbon content accelerates the melting of steel and lowers the melting point. Moreover, the order of melting points was found to be consistent with that of the stability of Fe_xC_y, that is, the stability gradually increases as the carbon concentration decreases.[78,79]

3.2. Melting Mechanism and Structural Evolution

The melting process of monometallic nanoparticles starts on the particle shell or surface and then extends to the entire particle.[21-24] The melting behaviors of bimetallic and multimetallic heterogeneous nanoparticles are more complicated due to their different element compositions and structural constructions.[58,80-82] The melting behaviors of the binary metal-nonmetal Fe_xC_y nanoparticles have not systematically investigated yet. As the important active phases in Fischer-Tropsch synthesis, Fe_xC_y nanoparticles are under the influence of large amounts of reaction heat released from the catalytic reaction and are subject to the rapid temperature increases. It will lead to partial or even total melting of the catalyst, thereby affecting the catalytic properties. Therefore, the melting mechanism and structure evolution of Fe_xC_y nanoparticles during heating are explored in this section.

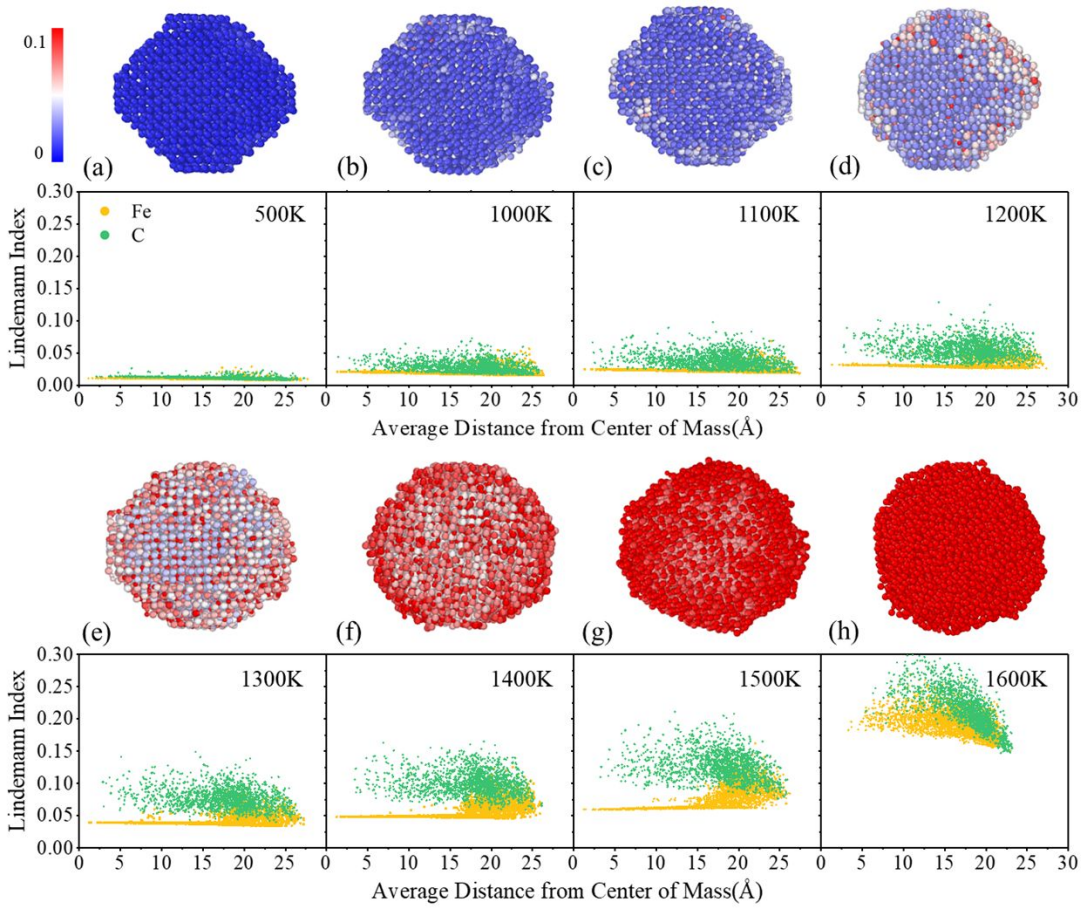

Fig. 3. Individual atom Lindemann index variation from a lower temperature to higher of 5 nm Fe_5C_2 nanoparticle. Large spheres and small spheres represent Fe atoms and C atoms, respectively.

Fig. 3 shows the radial distribution of the Lindemann indexes of all atoms in a 5 nm Fe_5C_2 nanoparticle at different temperatures, averaged over the trajectories of the MD simulations. At low temperatures, such as 500 K, the Lindemann indexes of all atoms are quite low, indicating that they only vibrate around their initial positions. The Lindemann indexes increase with the increase of temperature. Some surface atoms are activated and migrate to other positions as heated to 1200 K and show Lindemann index greater than 0.1. (Fig. 3d and Fig. S1) The nanoparticles undergo surface pre-melting and are in the solid-liquid coexistence state. As the temperature further increased, the number of migrating atoms gradually increases. (Fig. 3e-h) C atoms are more sensitive to temperature than Fe atoms.[83] At 1500 K, almost all C atoms are activated, while the internal Fe atoms remain inactivated, suggesting that the C atoms can be fully activated before the melting point reached, and the internal Fe atoms maintain the crystal

structure. As the temperature increased to the critical point, (Fig. 3h) the Lindemann index of inner Fe atoms suddenly increases, rising above 0.1, and the nanoparticles are completely melted. In addition, both 3 nm and 8 nm nanoparticles exhibit well-defined melting processes, while the process of 2 nm ones are indeed less clear. (Fig. S6) This is due to the smaller atomic number and larger surface-to-volume ratio of small-sized particle, which makes it difficult to form a stable solid core inside to resist high temperatures. After the surface pre-melting occurs, it is completely melted in a shorter temperature range. The narrow solid-liquid coexistence range of small nanoparticles leads to a lower melting temperature. These deductions indicate that the high temperature causes the phase transition of Fe_xC_y nanoparticles from solid to amorphous state.

The Lindemann index variations of the individual atom of other Fe_xC_y nanoparticles were also investigated. Those nanoparticles show similar melting behaviors that the C atoms are more easily activated than Fe atoms during the heating process. (Fig. S7-S9) As the carbon content decreases, the solid-liquid coexistence phenomenon is more obvious and the coexistence temperature range is larger, which is reflected in the increase of melting point. We speculate that the carbon content affects the melting temperature of Fe_xC_y nanoparticles from two aspects. First, at the activation temperature, the activated C atoms transfer excess kinetic energy to the Fe atoms to accelerate the melting of Fe.[33] Second, the melting point of structurally ordered nanoparticle is higher and thus its thermal stability is better than the disordered one.[84,85] High carbon contents increase the degree of disorder of Fe_xC_y lattice, and thus lower the melting point to facilitate the melting process.

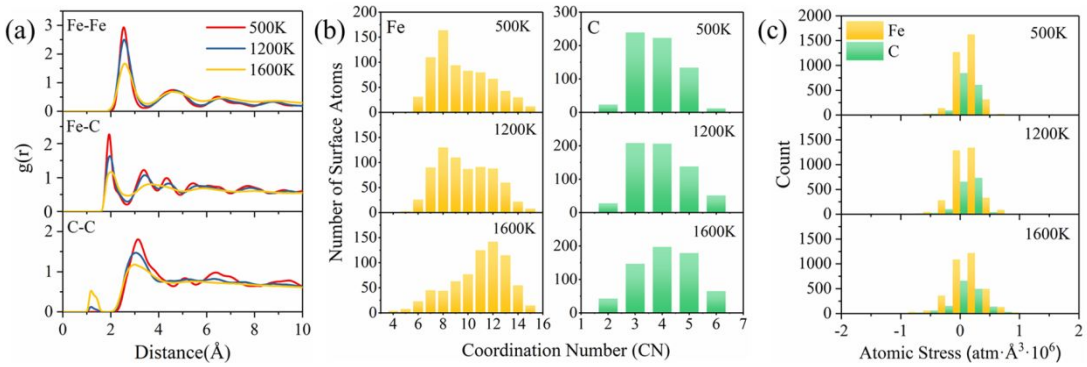

Fig. 4. Radial distribution functions of surface atoms (a), coordination numbers of surface atoms (b), and atomic stress distributions (c) of 5 nm Fe_5C_2 nanoparticles.

The specific melting process of binary Fe_xC_y nanoparticles characterized by the radial distribution function (RDF) and coordination numbers (CN) to determine the influences of temperature on their structure, 5 nm Fe_5C_2 nanoparticles are taken as an example for analyses below. The surface atoms of the 5 nm Fe_5C_2 equilibrium structure at 300 K are obtained by the method reported by Barron et al.[26] RDF is an important tool used to determine the structural properties of a material. It can provide more information for better understanding the melting process than Lindemann index. The RDFs of three pairs of atoms are calculated. As shown in Fig. 4a, the pair interactions between the surface atoms gradually become weaker with the increase of temperature. It should be noted that there are no neighboring C atoms in the Fe_5C_2 crystal at low temperatures. However, a tiny peak appears around 1.15 Å at 1200 K, indicating the possible formation of C-C bonds after surface pre-melting. The peak becomes significantly stronger at 1600 K, which suggests the occurrence of the aggregation of C atoms on surface. Fig. 4b shows the distributions of the CN of Fe and C atoms at different temperatures. At 500 K, the surface Fe atoms are mostly in 8-fold coordination form, and the high-fold coordination (CN > 12) Fe atoms are relatively rare. As the temperature is increased to over the pre-melting point, the coordination number of surface atoms changes dramatically. Owing to a completely melt of the entire nanoparticle at 1600 K, the internal and surface atoms undergo violent atomic exchange. The surface atoms at low temperatures may become internal atoms at high temperatures.[33] Therefore, the overall coordination number of surface Fe atoms is prone to increase with the increase of temperature, showing a shift of uniform distribution centered around 8 at 500 K to 12 at 1600 K. Carbon atoms exhibit a similar pattern. But this does not mean that the overall activity of the catalyst is reduced, as shown in Fig. 5c. The atomic stress distribution becomes obviously broader with the increase of temperature. (Fig. 4c) The kinetic energy of atoms rises with the increase of temperature, which causes structural expansion and greater internal stresses.[86] The increased kinetic

energy drives atomic exchange to form internal higher-fold coordination of atoms and generate superior internal stresses, which further weakens the RDF distribution of atomic pairs.

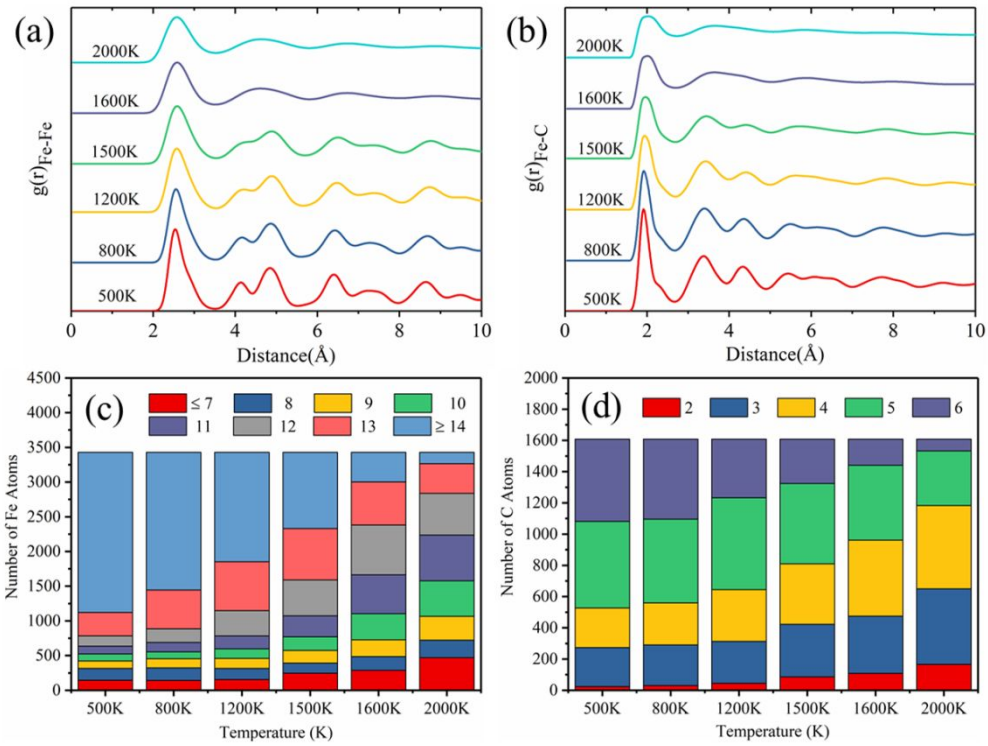

Fig. 5. Radial distribution function profiles of (a) Fe-Fe and (b) Fe-C in Fe_5C_2 nanoparticles at different temperatures; distributions of coordination numbers of the Fe atoms (c) and C atoms (d) in Fe_5C_2 nanoparticles at different temperatures.

Fig. 5 shows the RDF of all atoms in 5 nm Fe_5C_2 nanoparticles at different temperatures. The first peak of the RDF of all Fe atoms at 500 K is observed at ~2.55 Å, which is consistent to that reported in literatures[87] and the structural characteristics of bulk Fe_5C_2. (Fig. S10) The cut-off distance of the first coordination layer of Fe atoms (~2.55 Å) is irrelevant with temperature and particle size, and the main peaks become wider and weaker as the temperature increased. The minor peaks become inconspicuous as the temperature increased to 1200 K, and the second and the third peaks tend to merge into one. It corresponds exactly to the RDF peak pattern of Fe atoms on the surface and is a signal for the onset of surface melting. All peaks outside the first coordination layer disappears at 1600 K, indicating that the nanoparticle is completely

melted. For the RDF between Fe-C atoms, the first peak at 500 K is located at ~1.95 Å, consistent with that reported literature[87] and the structure of bulk Fe_5C_2. The changing trend of RDF with temperature is similar to that of Fe-Fe due to the gradual cleavage of Fe-C bonds. The broadening of the main RDF peaks and the vanishing of the minor RDF peaks are the major features of the solid-liquid phase transition process of nanoparticles.[80] The melting points derived from RDF measurements are consistent with those obtained by the Lindemann index analysis. Overall, the atomic coordination number shows a decrease trend for high-fold coordination atoms and an increase trend for low-fold coordination atoms with the increase of temperature. (Fig. 5c and 5d) It can be explained that more surface atoms are produced as the lattice expands under the internal stress during surface melting.

3.3. Atomic diffusion behavior during heating

As mentioned above, in addition to the thermal evolution during heating, the atomic diffusion properties are also important to the melting process of Fe_xC_y nanoparticles. Here, atomic diffusion analysis is used to further characterize the effect of temperature on structure. In general, the atomic diffusion rate rapidly increases with the increase of temperature, which inevitably leads to the redistribution of the components in the binary nanoparticles, and eventually changes the bulk structure and surface morphology and thereby affects all aspects of the properties of the nanoparticles. Therefore, the diffusion behaviors of atom are crucial for studying the performances of binary nanoparticles at different temperatures.

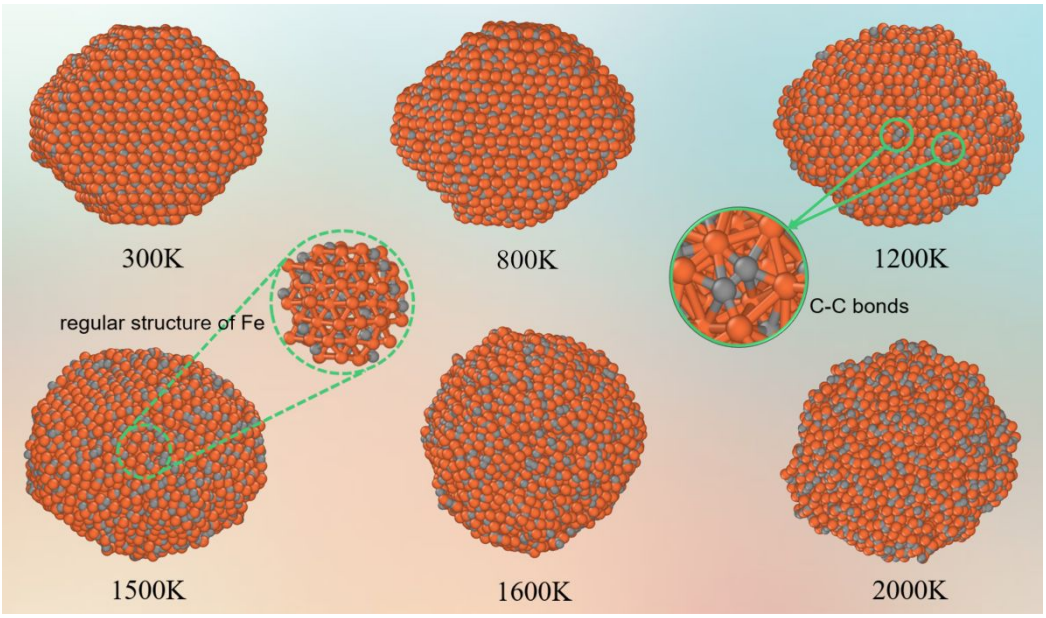

Fig. 6. Structure evolution of a 5 nm Fe_5C_2 nanoparticle with increasing temperature (orange: Fe; grey: C).

Fig. 6 shows snapshots of the atomic configurations of 5 nm nanoparticles at different temperatures. At the low-temperature intervals in the range from 300 K to 1200 K, the Wulff structure of the nanoparticle shows no significant changes. As the temperature arisen to 1200 K, the arrangements of some surface C atoms become irregular. Some edges and corners disappear due to the local morphological changes. A certain number of surface C atoms leave their original equilibrium positions and migrate, and some of them even neighbor with each other to form C-C bonds (green circles in Fig. 6). A large number of internal C atoms diffuse to the surface at 1500 K. Meanwhile, the internal Fe atoms remain in position as a core to maintain the regular crystal structure (dashed circle in Fig. 6). Further increasing the temperature to 1600 K causes the fierce transformation of the nanoparticle to a completely amorphous phase. The Fe_5C_2 nanoparticles surface begin to accumulate carbon atoms after surface pre-melting occurs. The di-carbon (C2) on the surface of the nanoparticles increases with the rising temperature, especially after melting. It may be the main cause of deactivation in the high-temperature Fischer-Tropsch process.[88,89]

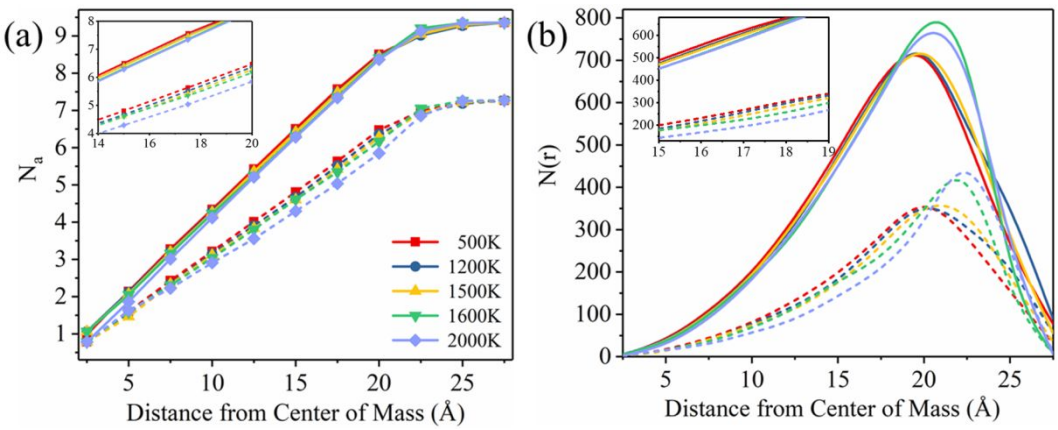

Fig. 7. (a) The axial distribution of atoms and (b) the atomic distribution functions of Fe_5C_2 at five representative temperatures. The solid lines represent Fe, and the dashed lines represent C.

The detailed diffusion behaviors of the atoms in Fe_5C_2 nanoparticles at different temperatures are presented in Fig. 7a. To simplify the statistical analysis, the Fe and C atoms are averaged to an axis by the volume formula of sphere. The axial distribution is defined as $N_a = \sqrt[3]{\frac{N_r}{\frac{4}{3}\pi}}$,[90] where N_r is the total number of atoms within the r distance from the center of mass and N_a is the corresponding average number of the atoms distributed along the axis. As can be seen from Fig. 7a, the distribution of carbon atoms along the axis at 500 K is linear, indicating that there is no obvious diffusion behavior below the pre-melting point. The axial distribution of atoms at ~ 20 Å from the center of mass gradually becomes flat because the nanoparticle is not a sphere and the axis partially reaches the surface at this point. As the temperature increased to 1200 K, the curve goes downward slightly, suggesting that the pre-melting point is reached. The internal atoms tend to diffuse outward because the activated surface atoms transfer their excess kinetic energy towards the internal structure of the nanoparticle. The downtrend of the curve becomes dramatic when the temperature is close to the melting point. A large number of internal carbon atoms are activated at the high temperature, and atomic exchange between the inner and outer layers becomes more frequent. The internal carbon atoms tend to diffuse outward and continuously segregate to the surface. The iron atoms maintain the framework of the nanoparticle, and thus migrate in smaller migration ranges than C atoms at the high temperatures. As shown in Fig. 7a, the

number of the internal Fe atoms remains almost consistent near the melting point. Although the Fe atoms also display thermal diffusion at high temperatures, they do not migrate outward as much as the C atoms do. The distribution of Fe atoms increases to a certain extent at 22.5 Å away from the center of mass because the core structure is destroyed at the melting point. All of the surface edges and corners disappear, and the nanoparticles are amorphized. (Fig. 6)

Table 1. The Fe/C ratio of 5nm Fe_5C_2 nanoparticle in the shell at different distances from the center of mass.

	Interior			**Near the Surface**	**Surface**
R (Å) / T (K)	**0 ~ 5**	**5 ~ 10**	**10 ~ 15**	**15 ~ 20**	**> 20**
500	2.5	2.5	2.5	2.1	1.8
1200	2.5	2.5	2.6	2.2	1.7
1500	2.8	2.5	2.8	2.2	1.6
1600	2.1	2.8	2.5	2.5	1.5
2000	1.5	3.1	3.3	2.8	1.3

The atomic distribution function *N(r)* of the Fe and C atoms in the nanoparticles were calculated to determine their distributions at different temperatures. *N(r)dr* is the number of atoms within a shell of thickness *dr* at the distance *r* from the center of mass.[91] As shown in Fig. 7b, the *N(r)dr* peak of C atom gradually shifts to right with the increase of temperature, which confirms the conclusion drawn above that C atoms tend to diffuse outward at high temperatures. The peak position shifts and the peak intensity increases dramatically at 1600 K, suggesting that the phase transition has completed. The *N(r)dr* peak of Fe atom shifts slightly to the right before the critical temperature reached because of the structural expansion caused by kinetic energy and atomic stress at the high temperatures. The peak shape also changes significantly at the melting point because of the migration and rearrangement of external atoms. To explain the diffusion behaviors of atom more clearly, the temperature dependence of Fe/C ratio in each shell is also calculated and summarized in Table 1. As can be seen, the internal Fe/C ratio gradually increases with the increase of temperature, up to more than 3 at 2000 K, and the surface Fe/C ratio decreases. In addition, the slope of mean square

displacements (MSD) and the diffusion coefficients gradually increase as the temperature rises, indicating that the diffusion rates of Fe and C atoms accelerate during heating. (Fig. S11) It should be noted that the diffusion coefficient of C atoms is always greater than that of Fe atoms, and the difference between the two becomes larger and larger after reaching the pre-melting point. This provides support for the outward diffusion behavior of C atoms. These results further suggest that the C atoms in the iron carbide nanoparticle tend to diffuse outwards at high temperatures and segregate and aggregate on the surface.

3.4 Catalytic Performance of Melted Nanoparticles

As mentioned above, the structural evolution of Fe_xC_y nanoparticles with increasing temperature is mainly manifested in the decrease of atomic coordination number and the accumulation of C atoms on the surface. The former provides more active sites for catalytic reactions, while the latter hinders the local adsorption of gas molecules.[92] In addition, it has been reported that both C and Fe atoms have catalytic activity for CO.[93-95] Therefore, the activity of melted nanoparticles needs to be further explored.

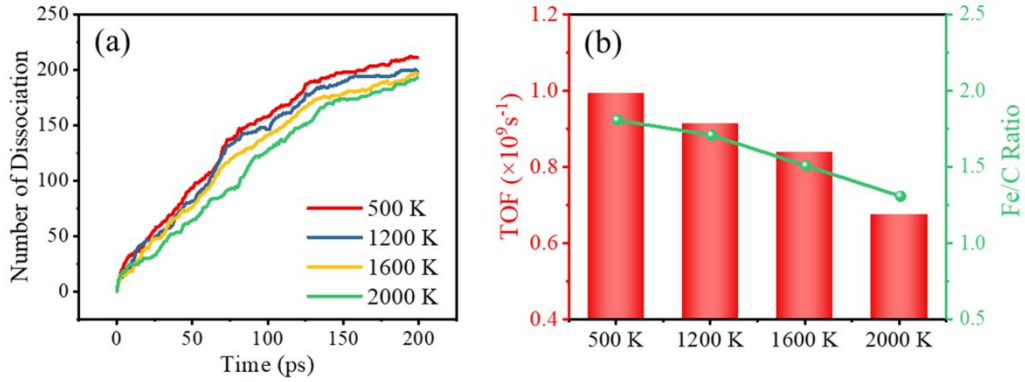

Fig. 8. (a) Curves of CO dissociation number with time, (b) the TOF values and surface Fe/C ratios for Fe_5C_2 nanoparticle at different temperatures.

CO dissociation is the critical step in the Fischer−Tropsch reaction.[38,39] To understand the effect of melting on the catalytic activity of Fe_xC_y nanoparticles, its catalytic performance represented by CO dissociation behaviors before and after

melting was examined. As shown in Fig. 8a, the CO dissociation number assumed temperature dependent on the nanoparticles throughout the 200 ps reaction. That is, the number of CO dissociation catalyzed by nanoparticles is more less after higher temperature treatment. The turn-over frequency (TOF) is one of the key indicators for assessing the catalytic activity, which is defined as: $TOF = N / M / T$, where N represents the amount of CO dissociation, M represents the number of surface atoms (Fe and C atoms) approximating the number of surface sites, and t represents the reaction time [69]. It was inferred from the inflection point in Fig. 8a that the gas pressure drops rapidly near 125 ps, so we used 125 ps as the reaction time in order to eliminate the influence of the pressure difference. Fig. 8b shows that the melted nanoparticles have lower TOF values compared to the unmelted ones. Moreover, the surface Fe/C ratio decreases due to the segregation of C atoms to the surface with increasing temperature. The TOF value was positively correlated with the surface Fe/C ratio. However, it should be pointed out that there is no hydrogen added to generate hydrocarbons. In actual catalytic reactions, the formation of hydrocarbons may lead to more complex situations.[39,44]

According to Fig. 6, the aggregation of carbon on the surface of the nanoparticles mainly exists in the form of C2. To further explore the effect of the presence of surface C2 on CO dissociation, we assumed that the surface C2 were removed in the form of olefins, and the melted nanoparticles without C2 on the surface (removed 111 pairs for 1600 K and 262 pairs for 2000 K) were reacted with CO under the same conditions. As shown in Fig. S12, the CO dissociation curves of the nanoparticles after removal of C2 were all higher than those before removal. The TOF values of nanoparticles without C2 is also higher than that of untreated nanoparticles (1600 K: 1.10 vs. 0.838; 2000 K: 1.17 vs. 0.674), and even higher than that of unmelted nanoparticles (500 K: 0.992; 1200 K: 0.914). Therefore, melting of surface at high temperatures can increase the catalytic activity of Fe_xC_y, but an important prerequisite is to control the aggregation of relatively weak carbon atoms in a hydrogen-deficient atmosphere. The carbon accumulation in the form of C2 on the surface at high temperature blocks the surface catalytic active sites, reducing activity of melted Fe_xC_y nanoparticles.

4. Conclusion

The melting behaviors and mechanisms of binary Fe_xC_y nanoparticles with different Fe/C ratios and different sizes were investigated by RMD simulations. We introduced the Lindemann index as an indicator of solid-liquid phase transition and determined the melting points and surface pre-melting points for different nanoparticles. The critical point of melting temperature increases with the increase of particle size. Both the melting temperature and the pre-melting temperature have a good linear relationship with the inverse of the nanoparticle size. For the Fe_xC_y nanoparticles of similar sizes, the higher the C content, the lower the melting point. The melting process largely occurs from surface to internal, but it should be noted that the C atoms are always fully activated before reaching the melting point, while the inner core region, composed of Fe atoms, melts abruptly only when the critical temperature is reached. The C atoms are more sensitive to temperature than Fe atoms and exhibit temperature-dependent thermal diffusion behaviors. They tend to diffuse outward and accelerate its structure evolution. At the same time, it can aggregate on the surface of nanoparticle at high temperatures. Such carbon accumulation in the form of C2 clogs the surface-active sites and leads to a lower TOF value of Fe_xC_y nanoparticles for CO dissociation. Our work sheds light on the melting mechanism, surface pre-melting, and atomic thermal diffusion of binary Fe_xC_y nanoparticles on the atomic level. More important, C2 maybe the key intermediate in the CO activation process, whose contents determines the surface activity of the catalyst. We hope that these findings could provide some enlightenment for the possible controllable structural evolution of Fe_xC_y in catalytic reactions.

Corresponding Author

* Yu-Fei Song (E-mail: songyf@mail.buct.edu.cn, ORCID: 0000-0003-1309-0626)

* Xiao-Dong Wen (E-mail: wxd@sxicc.ac.cn, ORCID: 0000-0001-5626-8581)

* Kuan Lu (E-mail: lukuan@sxicc.ac.cn, ORCID: 0000-0002-8593-2768)

Conflicts of interest

The authors declare no competing financial interest.

Acknowledgments

The authors are grateful for the financial support from the National Natural Science Foundation of China (No. 21625101, No. 21972157, and No. 21972160), Fundamental Research Funds for the Central Universities (XK1802-6), CAS Project for Young Scientists in Basic Research(YSBR-005), and funding support from Synfuels China, Co. Ltd and "Transformational Technologies for Clean Energy and Demonstration", Strategic Priority Research Program of the Chinese Academic of Sciences (No. XDA 21000000). We also acknowledge the innovation foundation of the Institute of Coal Chemistry, Chinese Academy of Sciences, Hundred-Talent Program of Chinese Academy of Sciences, Shanxi Hundred-Talent Program, and National Thousand Young Talents Program of China.

References

1 S. U. Son, Y. Jang, J. Park, H. B. Na, H. M. Park, H. J. Yun, J. Lee and T. Hyeon, *J. Am. Chem. Soc.*, 2004, **126**, 5026-5027.

2 L. Lu, J. Liu, Y. Hu, Y. Zhang and W. Chen, *Adv. Mater.*, 2013, **25**, 1270-1274.

3 A. Kryshtal, A. Minenkov, S. Bogatyrenko and A. Gruszczyński, *J. Alloys Compd.*, 2019, **786**, 817-825.

4 C. Cui, L. Gan, M. Heggen, S. Rudi and P. Strasser, *Nat. Mater.*, 2013, **12**, 765-771.

5 M. Takagi, *J. Phys. Soc. JPN*, 2007, **9**, 359-363.

6 K. Dick, T. Dhanasekaran, Z. Zhang and D. Meisel, *J. Am. Chem. Soc.*, 2002, **124**, 2312-2317.

7 K. Nanda, *Pramana*, 2009, **72**, 617-628.

8 Y. Gao, C. Zou, B. Yang, Q. Zhai, J. Liu, E. Zhuravlev and C. Schick, *J. Alloys Compd.*, 2009, **484**, 777-781.

9 C. Gao, F. Lyu and Y. Yin, *Chem. Rev.*, 2020, **121**, 834-881.

10 Z. Li, S. Ji, Y. Liu, X. Cao, S. Tian, Y. Chen, Z. Niu and Y. Li, *Chem. Rev.*, 2019, **120**, 623-682.

11 L. Liu and A. Corma, *Chem. Rev.*, 2018, **118**, 4981-5079.

12 M. Böyükata, E. Borges, J. P. Braga and J. C. Belchior, *J. Alloys Compd.*, 2005, **403**, 349-356.

13 U. Domekeli, S. Sengul, M. Celtek and C. Canan, *Philos. Mag.*, 2017, **98**, 371-387.

14 R. Essajai, A. Rachadi, E. Feddi and N. hassanain, *Mater. Chem. Phys.*, 2018, **218**, 116-121.

15 J. Liu, M. Wang and P. Liu, *Mater. Res. Express*, 2018, **5**, 065011.

16 Saman, Alavi, Donald, L. and Thompson, *J. Phys. Chem. A*, 2006, **110**, 1518-1523.

17 J. Xie, H. M. Torres Galvis, A. C. Koeken, A. Kirilin, A. I. Dugulan, M. Ruitenbeek and K. P. de Jong, *ACS Catal.*, 2016, **6**, 4017-4024.

18 J. Xie, J. Yang, A. I. Dugulan, A. Holmen, D. Chen, K. P. de Jong and M. J. Louwerse, *ACS Catal.*, 2016, **6**, 3147-3157.

19 Z. Schnepp, S. C. Wimbush, M. Antonietti and C. Giordano, *Chem. Mater.*, 2010, **22**, 5340-5344.

20 S. Mahadik-Khanolkar, S. Donthula, A. Bang, C. Wisner, C. Sotiriou-Leventis and N. Leventis, *Chem. Mater.*, 2014, **26**, 1318-1331.

21 J. Sun, P. Liu, M. Wang and J. Liu, *Sci. Rep.*, 2020, **10**, 1-11.

22 Q. Shu, Y. Yang, Y. T. Zhai, D. Y. Sun, H. J. Xiang and X. G. Gong, *Nanoscale*, 2012, **4**, 6307-6311.

23 F. Ding, K. Bolton and A. Rosén, *Eur. Phys. J. D*, 2005, **34**, 275-277.

24 N. P. Joshi, D. E. Spearot and D. Bhat, *J. Nanosci. Nanotechnol.*, 2010, **10**, 5587-5593.

25 S. K. Matam, E. V. Kondratenko, M. H. Aguirre, P. Hug, D. Rentsch, A. Winkler, A. Weidenkaff and D. Ferri, *Appl. Catal. B-Environ.*, 2013, **129**, 214-224.

26 H. Barron, G. Opletal, R. D. Tilley and A. S. Barnard, *Catal. Sci. Technol.*, 2016, **6**, 144-151.

27 S. Vajda, S. Lee, K. Sell, I. Barke, A. Kleibert, V. von Oeynhausen, K. H. Meiwes-Broer, A. F. Rodriguez, J. W. Elam, M. M. Pellin, B. Lee, S. Seifert and R. E. Winans, *J. Chem. Phys.*, 2009, **131**, 121104.

28 X.-Q. Zhang, E. Iype, S. V. Nedea, A. P. J. Jansen, B. M. Szyja, E. J. M. Hensen and R. A. van Santen, *J. Phys. Chem. C*, 2014, **118**, 6882-6886.

29 M. N. Krstajić Pajić, S. I. Stevanović, V. V. Radmilović, A. Gavrilović-Wohlmuther, V. R. Radmilović, S. L. Gojković and V. M. Jovanović, *Appl. Catal. B-Environ.*, 2016, **196**, 174-184.

30 M. P. Suárez and D. G. Löffler, *J. Catal.*, 1986, **97**, 240-242.

31 P. Tang, Q. Zhu, Z. Wu and D. Ma, *Energy Environ. Sci.*, 2014, **7**, 2580-2591.

32 V. Sadykov, L. Isupova, I. Zolotarskii, L. Bobrova, A. Noskov, V. Parmon, E. Brushtein, T. Telyatnikova, V. Chernyshev and V. Lunin, *Appl. Catal. A-Gen.*, 2000, **204**, 59-87.

33 X. Liu, X. Wen and R. Hoffmann, *ACS Catal.*, 2018, **8**, 3365-3375.

34 Y.-K. Dou, H. Cao, X.-F. He, J. Gao, J.-l. Cao and W. Yang, *J. Alloys Compd.*, 2021, **857**.

35 N. Yan, L. Qin, H. Hao, L. Hui, F. Zhao and H. Feng, *Appl. Surf. Sci.*, 2017, **408**, 51-59.

36 C. Ni, H. Ding and X. J. Jin, *J. Alloys Compd.*, 2013, **546**, 1-6.

37 J. Yang, W. Hu and J. Tang, *RSC Adv.*, 2013, **4**, 2155-2160.

38 C. Yang, H. Zhao, Y. Hou and D. Ma, *J. Am. Chem. Soc.*, 2012, **134**, 15814-15821.

39 Y. Li, Z. Li, A. Ahsen, L. Lammich, G. J. A. Mannie, J. W. H. Niemantsverdriet and J. V. Lauritsen, *ACS Catal.*, 2018, **9**, 1264-1273.

40 K. Lu, C.-F. Huo, Y. He, W.-P. Guo, Q. Peng, Y. Yang, Y.-W. Li and X.-D. Wen, *J. Catal.*, 2019, **374**, 150-160.

41 E. de Smit, F. Cinquini, A. M. Beale, O. V. Safonova, W. van Beek, P. Sautet and B. M. Weckhuysen, *J. Am. Chem. Soc.*, 2010, **132**, 14928-14941.

42 L. Zhu, *Applied Sciences*, 2005.

43 Y.-g. C. Keiichi Tomishige, Kaoru Fujimoto, *J. Catal.*, 1999, **181**, 91–103.

44 M. O. Ozbek and J. W. Niemantsverdriet, *J. Catal.*, 2014, **317**, 158-166.

45 D. C. L. Peter E. Nolan, Andrew Hall Cutler, *J. Phys. Chem. B*, 1998, **102**, 4165-4175.

46 R. Haldeman and M. Botty, *J. Phys. Chem.*, 1959, **63**, 489-496.

47 P. S. Ghosh, K. Ali, A. Vineet, A. Voleti and A. Arya, *J. Alloys Compd.*, 2017, **726**, 989-1002.

48 W. Ge, W. Gao, J. Zhu and Y. Li, *J. Alloys Compd.*, 2019, **781**, 1069-1073.

49 K. Jack, *Acta Crystallogr.*, 1950, **3**, 392-394.

50 C. K. Ande and M. H. Sluiter, *Metall. Mater. Trans. A*, 2012, **43**, 4436-4444.

51 X. Chong, Y. Jiang and J. Feng, *J. Alloys Compd.*, 2018, **745**, 196-211.

52 A. K. Biswas, *Indian J. Hist. Sci.*, 1994, **29**, 579-610.

53 E. de Smit, I. Swart, J. F. Creemer, G. H. Hoveling, M. K. Gilles, T. Tyliszczak, P. J. Kooyman, H. W. Zandbergen, C. Morin, B. M. Weckhuysen and F. M. de Groot, *Nature*, 2008, **456**, 222-225.

54 H. J. Hoffmann, *Materialwiss. Werkst.*, 2004, **35**, 79-81.

55 K. Zhang, G. M. Stocks and J. Zhong, *Nanotechnology*, 2007, **18**, 285703.

56 Q. S. Mei and K. Lu, *Prog. Mater. Sci.*, 2007, **52**, 1175-1262.

57 Y. Engelmann, A. Bogaerts and E. C. Neyts, *Nanoscale*, 2014, **6**, 11981-11987.

58 Y. H. Wen, L. Li, Y. M. Li and R. Huang, *J. Phys. Chem. Lett.*, 2021, **12**, 2454-2462.

59 H. Löwen, *Phys. Rep.*, 1994, **237**, 249-324.

60 K. Hansen, *Statistical Physics of Nanoparticles in the Gas Phase*, 2013.

61 A. C. T. van Duin, S. Dasgupta, F. Lorant and W. A. Goddard, *J. Phys. Chem. A*, 2001, **105**, 9396-9409.

62 L. Liu, A. Jaramillo-Botero, W. A. Goddard and H. Sun, *J. Phys. Chem. A*, 2012, **116**, 3918-3925.

63 G. Wulff, *Z. Kristallogr*, 1901, **34**, 449-530.

64 S. Zhao, X.-W. Liu, C.-F. Huo, Y.-W. Li, J. Wang and H. Jiao, *J. Catal.*, 2012, **294**, 47-53.

65 S. Zhao, X.-W. Liu, C.-F. Huo, Y.-W. Li, J. Wang and H. Jiao, *Catal. Struct. React.*, 2014, **1**, 44-60.

66 S. Plimpton, *J. Comput. Phys.*, 1995, **117**, 1-19.

67 Stukowski and Alexander, *Model. Simul. Mater. Sc.*, 2010, **18**, 2154-2162.

68 K. Lu, Y. He, C.-F. Huo, W.-P. Guo, Q. Peng, Y. Yang, Y.-W. Li and X.-D. Wen, *J. Phys. Chem. C*, 2018, **122**, 27582-27589.

69 K. Lu, D. Luo, Y. He, C.-F. Huo, Y. Zhou, W.-P. Guo, Q. Peng, Y. Yang, Y.-W. Li and X.-D. Wen, *Appl. Surf. Sci.*, 2021, **570**, 151018.

70 S. L. Lai, J. Y. Guo, V. Petrova, G. Ramanath and L. H. Allen, *Phys. Rev. Lett.*, 2010, **77**, 99-102.

71 A. P. Chernyshev, *Mater. Lett.*, 2009, **63**, 1525-1527.

72 V. S. Tsepelev, Y. N. Starodubtsev, K. M. Wu and Y. A. Kochetkova, *Key. Eng. Mater.*, 2020, **861**, 107-112.

73 F. Font, T. G. Myers and S. L. Mitchell, *Microfluid. Nanofluid.*, 2014, **18**, 233-243.

74 G. Fiquet, J. Badro, E. Gregoryanz, Y. Fei and F. Occelli, *Phys. Earth Planet. In.*, 2009, **172**, 125-129.

75 K. D. Litasov, I. S. Sharygin, P. I. Dorogokupets, A. Shatskiy, P. N. Gavryushkin, T. S. Sokolova, E. Ohtani, J. Li and K. Funakoshi, *J. Geophys. Res. Solid Earth*, 2013, **118**, 5274-5284.

76 O. T. Lord, M. J. Walter, R. Dasgupta, D. Walker and S. M. Clark, *Earth Planet Sci. Lett.*, 2009, **284**, 157-167.

77 X. Xi, S. Li, S. Yang, M. Zhao and J. Li, *Ironmak. Steelmak.*, 2020, **47**, 1087-1099.

78 G. Raupp and W. Delgass, *J. Catal.*, 1979, **58**, 337-347.

79 J. Amelse, J. Butt and L. Schwartz, *J. Phys. Chem.*, 1978, **82**, 558-563.

80 X. Zhang, B. Li, H. X. Liu, G. H. Zhao, Q. L. Yang, X. M. Cheng, C. H. Wong, Y. M. Zhang and C. W. J. Lim, *Appl. Surf. Sci.*, 2019, **465**, 871-879.

81 Y.-H. Wen, L. Li, T. Zhao and R. Huang, *ACS Appl. Nano Mater.*, 2020, **3**, 12369-12378.

82 M. Li and D. Cheng, *J. Phys. Chem. C*, 2013, **117**, 18746-18751.

83 P. Thibaux, A. Métenier and C. Xhoffer, *Metall. Mater. Trans. A*, 2007, **38**, 1169-1176.

84 Y.-H. Wen, L.-H. Zhang, J.-B. Wang and R. Huang, *J. Alloys Compd.*, 2019, **776**, 629-635.

85 Y.-H. Wen and R. Huang, *J. Phys. Chem. C*, 2019, **123**, 12007-12014.

86 X. Zhang, C. Fu, Y. Xia, Y. Duan, Y. Li, Z. Wang, Y. Jiang and H. Li, *ACS Nano*, 2019, **13**, 3005-3014.

87 M. Ruda, D. Farkas and G. Garcia, *Comput. Mater. Sci.*, 2009, **45**, 550-560.

88 J. Li, E. Croiset and L. Ricardez-Sandoval, *Phys. Chem. Chem. Phys.*, 2014, **16**, 2954-2961.

89 R. Gao, X. Liu, Z. Cao, X.-W. Liu, K. Lu, D. Ma, Y. Yang, Y.-W. Li, R. Hoffmann and X.-D. Wen, *Catal. Lett.*, 2019, **149**, 645-664.

90 A. Seidenberg, *Arch. Hist. Exact. Sci.*, 1988, **39**, 97-119.

91 R. Huang, Y.-H. Wen, G.-F. Shao, Z.-Z. Zhu and S.-G. Sun, *J. Phys. Chem. C*, 2013, **117**, 6896-6903.

92 D. C. Sorescu, *The Journal of Physical Chemistry C*, 2009, **113**, 9256-9274.

93 D.-B. Cao, F.-Q. Zhang, Y.-W. Li and H. Jiao, *J. Phys. Chem. B*, 2004, **108**, 9094-9104.

94 X.-Y. Liao, D.-B. Cao, S.-G. Wang, Z.-Y. Ma, Y.-W. Li, J. Wang and H. Jiao, *J. Mol. Catal. A: Chem.*, 2007, **269**, 169-178.

95 C.-M. Deng, C.-F. Huo, L.-L. Bao, G. Feng, Y.-W. Li, J. Wang and H. Jiao, *J. Phys. Chem. C*, 2008, **112**, 19018–19029.